

# AnimatableDreamer: Text-Guided Non-rigid 3D Model Generation and Reconstruction with Canonical Score Distillation

Xinzhou Wang<sup>1,2,3</sup> Yikai Wang<sup>2†</sup> Junliang Ye<sup>2</sup> Zhengyi Wang<sup>2,3</sup> Fuchun Sun<sup>2†</sup>  
 Pengkun Liu<sup>2,4</sup> Ling Wang<sup>2,5</sup> Kai Sun<sup>2</sup> Xintong Wang<sup>6</sup> Bin He<sup>1</sup>

<sup>1</sup>Tongji University <sup>2</sup>Tsinghua University <sup>3</sup>ShengShu

<sup>4</sup>Fudan University <sup>5</sup>Xi'an Research Institute of High-Tech <sup>6</sup>Zhejiang University

## Abstract

*Text-to-3D model adaptations have advanced static 3D model quality, but sequential 3D model generation, particularly for animatable objects with large motions, is still scarce. Our work proposes ANIMATABLEDREAMER, a text-to-4D generation framework capable of generating diverse categories of non-rigid objects while adhering to the object motions extracted from a monocular video. At its core, ANIMATABLEDREAMER is equipped with our novel optimization design dubbed Canonical Score Distillation (CSD), which simplifies the generation dimension from 4D to 3D by denoising over different frames in the time-varying camera spaces while conducting the distillation process in a unique canonical space shared per video. Concretely, CSD ensures that score gradients back-propagate to the canonical space through differentiable warping, hence guaranteeing the time-consistent generation and maintaining morphological plausibility across different poses. By lifting the 3D generator to 4D with warping functions, ANIMATABLEDREAMER offers a novel perspective on non-rigid 3D model generation and reconstruction. Besides, with inductive knowledge from a multi-view consistent diffusion model, CSD regularizes reconstruction from novel views, thus cyclically enhancing the generation process. Extensive experiments demonstrate the capability of our method in generating high-flexibility text-guided 3D models from the monocular video, while also showing improved reconstruction performance over typical non-rigid reconstruction methods. Project page <https://AnimatableDreamer.github.io/>.*

## 1. Introduction

Automatically building animatable 3D models with non-rigid deformations and motions plays a crucial role in broad

fields such as gaming, virtual reality, film special effects, etc. Recent efforts have been devoted to reconstructing animatable 3D models with pre-defined templates or multi-view reconstruction principles [12, 32, 43, 48, 51]. Nevertheless, these methods are mostly category-specific with limited diversity or largely rest on the captured data. [8, 33, 47]. With the remarkable success of deep generative models, generating various 2D images through text prompts comes to reality [25, 26, 52], and this success is expanding beyond 2D generation. The application of Score Distillation Sampling (SDS) [23] has elevated 2D text-to-image diffusion models to generate high-quality 3D models. Numerous subsequent works have emerged in this domain [16, 30, 34, 41]. However, generating deformable objects remains challenging due to their inherent unconstrained nature in high flexibility and non-rigidity.

Intuitively, compared to unconstrained warping field [20, 21, 37], articulation extracted by implicit animatable models could serve as a geometry guidance for the 3D generator. Simultaneously, distilling 2D priors from the diffusion model in various model poses serves to regularize the canonical model and avoid short-cut solutions [18]. We believe there exists a synergy between animatable generation and reconstruction, which potentially promotes performance for one another. In response, we propose **ANIMATABLEDREAMER**, a framework with the capability to generate generic categories of non-rigid 3D models. This two-stage framework first extracts articulations from a monocular video with a generative model as regularizer, and subsequently generates novel non-rigid 3D models based on extracted articulations and a given text prompt.

In this context, we disentangle the non-rigid object into a differentiable implicit field in canonical space and an invertible neural skinning function [6, 17, 47, 48]. Specifically, we design **Canonical Score Distillation (CSD)** for our ANIMATABLEDREAMER, a novel SDS strategy that aims to attain the synergy of both animatable generation and reconstruction. Through invertible warping functions, CSD de-

† Corresponding Authors.

noises multiple camera spaces while consistently optimizing a static canonical space shared by all video frames. This novel approach simplifies 4D generation into a more manageable 3D process, yet maintains comprehensive supervision throughout the 4D space and ensures the morphological plausibility of the model under various object poses.

To summarise, we make the following contributions:

- **ANIMATABLEDREAMER:** A novel approach that unifies the generation and reconstruction of diverse non-rigid 3D models from monocular video. This is the first implementation of text-guided non-rigid 4D generation using video-based articulations, and a pioneering effort in monocular non-rigid reconstruction that leverages inductive priors from pre-trained 2D diffusion models.
- **Canonical Score Distillation:** A new distillation method blending non-rigid 3D generation and reconstruction. CSD back-propagates gradients from multiple camera spaces to a static canonical space, ensuring morphological plausibility throughout the 4D space.
- **Superior Experimental Results:** Our method excels in generating text-prompted 3D models with skeleton binding and outshines typical monocular non-rigid reconstruction method, especially in scenarios with limited viewpoints and large motion. Our generated diverse models can be manipulated and animated by controlling the rigid transformations of bones.

## 2. Related Work

### 2.1. Neural Reconstruction for 3D Non-rigid Object

The Neural Radiance Field (NeRF) has been a groundbreaking advancement in representing static scenes, enabling the generation of photorealistic novel views and detailed geometry reconstruction [1, 2, 15, 17]. Adapting NeRF for dynamic scenarios has involved augmenting the field into higher dimensions to accommodate objects with changing topologies [21]. An alternative strategy in dynamic object reconstruction employs an additional warping field to deform the NeRF [20, 24]. Nonetheless, these dynamic NeRF adaptations often encounter performance degradation, primarily due to the complexities introduced by the added temporal dimension. This could be alleviate by applying alternative representations including tesnors [28], Gaussian Splatting [42] and explicit representation [4, 11]. Despite these innovations, synthesizing space-time views from monocular perspectives remains a significant hurdle. Implementing spatio-temporal regularization methods, including depth and flow regularization, has shown potential in overcoming this issue [10, 44]. Furthermore, exploring category-specific or articulate priors offers promising avenues for reconstructing non-rigid objects [8, 22, 39, 47–49]. These methods present new opportunities and insights for the future of 3D non-rigid object reconstruction.

### 2.2. Distillation-based 3D Generation from Diffusion Model

SDS [23] has gained prominence for its capability to elevate pre-trained 2D diffusion models to the realm of 3D generation. By distillate 2D prior learned from large-scale datasets and optimize implicit field [17], SDS is able to generate high quality 3D model based on text-prompt [7, 36, 41]. The integration of differentiable marching tetrahedra [29] further enhances the combination of explicit meshes and SDS [16]. However, semantic consistency challenges arise in distillation-based 3D generation methods due to their disconnection from the 3D dataset during training. Addressing this concern, MVDream [30] introduces a multi-view diffusion model for panoramas with homography-guided attention, improving semantic consistency by incorporating cross-view attention and camera conditions. Further, 2D diffusion model trained can be lifted to 4D via a temporal score distillation sampling [31], which integrate world knowledge into 3D temporal representations.

## 3. Method

Given a monocular video of a deformable object belonging to class (e.g., cat, bird, squirrel), our objective is two-fold: first, to generate an object related to a specified prompt  $p$ , driven by the learned articulations and rigging from the provided video (Sec. 3.2); second, to reconstruct the original object (Sec. 3.4). We base our articulated model on the framework of BANMo [47] with some modifications (Sec. 3.1) and explore its potential in deformable object generation. The proposed ANIMATABLEDREAMER consists of two parallel workflows operating concurrently: generation (Sec. 3.2) and reconstruction (Sec. 3.4), as illustrated in Fig. 1. These workflows supervise the deformed model in **camera space** (articulated poses) and optimize the model in **canonical space** (rest pose) through differentiable warping. This approach aggregates information across various viewpoints and articulations, ensuring time consistency and plausible articulation.

### 3.1. Implicit Articulate Model

We adopt the BANMo framework [47] for our representation, primarily driven by two considerations. Firstly, leveraging self-supervised registration and priors from off-the-shelf methods [14, 19, 46], BANMo demonstrates potential in extracting articulations and models of generic-category objects from monocular videos. Secondly, in contrast to dense motion fields [4, 20, 21], BANMo disentangles non-rigid objects into a canonical model and a compact motion field with neural blend skinning. This disentanglement enables the application of distillation-based 3D generators. BANMo represents canonical model with 3D point color  $\mathbf{c} \in \mathbb{R}^3$  from NeRF [17], while modified it with a Signed

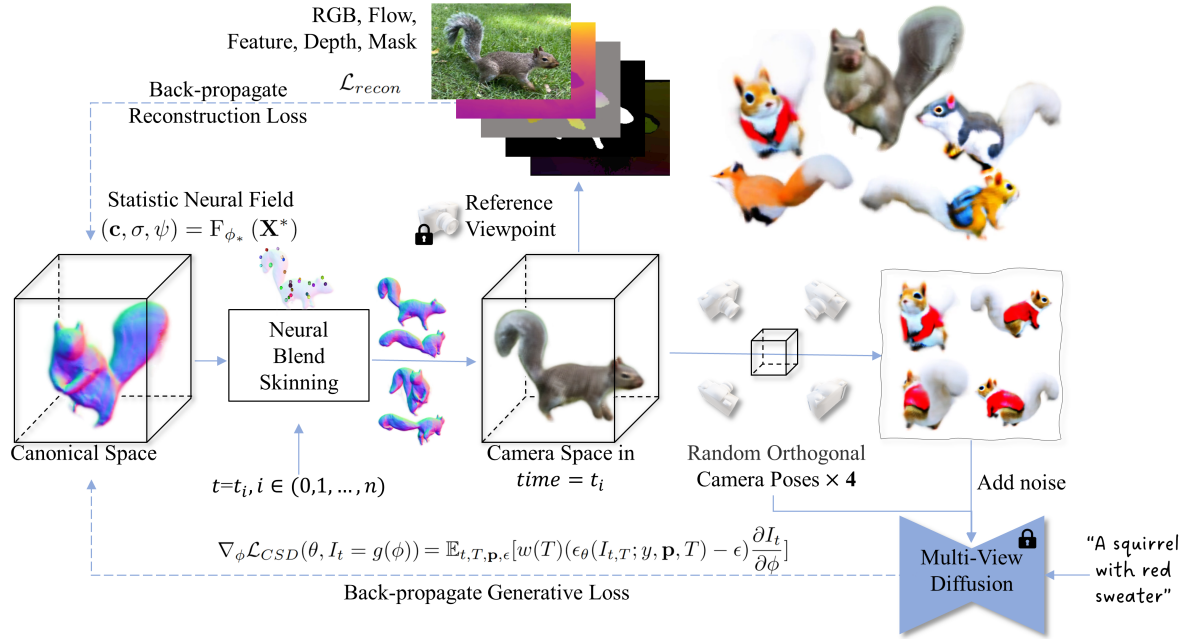


Figure 1. **Framework overview.** The articulate model consists of a static neural field and a time-varying neural skinning to transform the object from canonical space to camera space. During training, we optimized the model in camera space across different frames. For reconstruction flow, we compute loss with respect to reference images and pre-computed depth, flow and features. For generation flow, we employ spatiotemporal consistent score distillation sampling on four orthogonal views.

Distance Function (SDF) field to represent volume density  $\sigma \in (0, 1)$  and a feature descriptor  $\psi \in \mathbb{R}^{16}$  for 3D point registration:

$$\begin{aligned} \mathbf{c} &= \mathbf{MLP}_c(\mathbf{X}^*, \mathbf{v}), \\ \sigma &= \Gamma_\beta(\mathbf{MLP}_{SDF}(\mathbf{X}^*)), \\ \psi &= \mathbf{MLP}_\psi(\mathbf{X}^*), \end{aligned} \quad (1)$$

where  $\Gamma_\beta(\cdot)$  is the cumulative of a unimodal distribution, which converts SDF to density [38, 40].  $\psi$  is a feature descriptor based on 2D feature extracted from self-supervised vision model DINOV2 [19]. Considering that at each step, SDS supervises a point along the time axis without strong texture continuity constraints, we employ a time-invariant canonical model to prevent texture flickering. To warp the field from camera space to canonical space, BANMo builds the mapping between the 3D point in canonical space  $\mathbf{X}^*$  and 3D point in camera space  $\mathbf{X}^t$  with blend skinning deformation:

$$\mathbf{X}^t = \mathcal{W}_{\phi_w}^{t, \rightarrow}(\mathbf{X}^*) = \mathbf{G}^t(\mathbf{J}^{t, \rightarrow} \mathbf{X}^*), \quad (2)$$

$$\mathbf{X}^* = \mathcal{W}_{\phi_w}^{t, \leftarrow}(\mathbf{X}^t) = \mathbf{J}^{t, \leftarrow}((\mathbf{G}^t)^{-1} \mathbf{X}^t), \quad (3)$$

where root body transformation  $\mathbf{G}^t \in SE(3)$  is quaternion learned from  $\mathbf{MLP}_G$  related to time  $t$ . Weighted averages of bones transformation  $\mathbf{J}^{t, \rightarrow} \in SE(3)$ ,  $\mathbf{J}^{t, \leftarrow} \in SE(3)$  are quaternions learned from  $\mathbf{MLP}_J$  related to time  $t$ . Here we group the parameters of  $\mathbf{MLP}_G$  and  $\mathbf{MLP}_J$  as  $\phi_w$ . To render a pixel  $\mathbf{c}$  in camera space with respect to time  $t$ , we

warp camera space sampling points  $\mathbf{X}^t$  to canonical space with warping function and apply volume rendering:

$$\mathbf{c}(\mathbf{x}^t) = \mathcal{R}_{\phi*}(\mathcal{W}_{\phi_w}^{t, \leftarrow}(\mathbf{X}^t)), \quad (4)$$

where  $\phi_*$  are parameters of  $\mathbf{MLP}_c$ ,  $\mathbf{MLP}_{SDF}$  and  $\mathbf{MLP}_\psi$ , as defined in Eq. (1).  $R(\cdot)$  is pixel-level volume rendering function:

$$\mathcal{R}_{\phi*}(\mathcal{W}_{\phi_w}^{t, \leftarrow}(\mathbf{X}^t)) = \sum_{i=1}^N \tau_i \mathbf{c}(\mathcal{W}_{\phi_w}^{t, \leftarrow}(\mathbf{X}_i^t)). \quad (5)$$

where the  $i$ -th sampling point  $\mathbf{X}_i^t \in \mathbb{R}^3$  warped to canonical space point  $\mathbf{X}_i^*$ ,  $\mathbf{c}$  is pixel color,  $\tau_i$  is the visible probability of  $X_i^t$  computed by the density of warped sampling points  $\sigma_i = \sigma(\mathcal{W}_{\phi_w}^{t, \leftarrow}(\mathbf{X}_i^t))$ , as defined in Eq. (1).

### 3.2. Spatial Consistent Supervision

We distillate prior from diffusion model [5, 16, 23, 41] for reconstruction and generation with SDS. Unlike supervising with generated images, SDS takes a rendered image to predict a gradient towards a higher density region following the score function of the conditioned diffusion model. This gradient not only points to an image of higher quality but also maintains the content coherence of the rendered image. By taking the rendered image as input, the diffusion model narrows down the prior to the target instance.

This 2D supervision is sufficient for static object generation. However, in 4D reconstructing, supervising a single

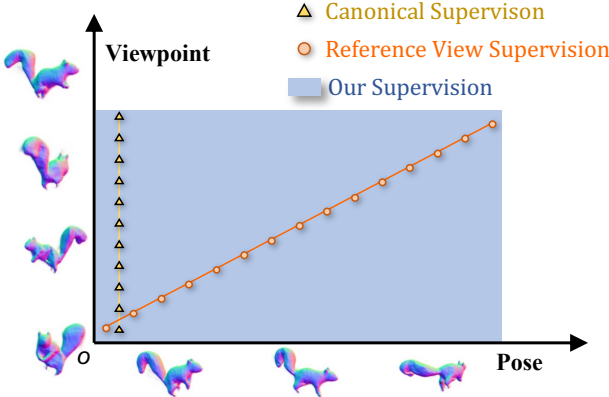


Figure 2. **CSD supervises the entire 4D space.** Our approach can traverse the entire XYZ-t space. In contrast, approaches that focus exclusively on the canonical space or solely on reference views are limited to supervising just a single hyperplane within this 4D space.

view at a single time point  $t$  becomes insufficient. As illustrated in Fig. 2, the supervision from the reference video forms a hyper-plane in the 4D space, resulting in lower quality for unobserved viewpoints. When denoising an image rendered from a viewpoint far away from reference with a large guidance scale, SDS tends to sample an new instance from its own distribution, due to the lack of sufficient information about the original instance (Fig. 5(b)). Here we incorporate multi-view consistent diffusion model MV-Dream [30], which is trained on a 3D dataset Objaverse [9] and a 2D dataset LAION [27] and is able to generate multi-view consistent images by taking camera poses as condition. The SDS loss of MVDream is defined as:

$$\nabla_{\phi} \mathcal{L}_{SDS}(\theta, I = g(\phi)) = \mathbb{E}_{T, p, \epsilon} [w(T)(\epsilon_{\theta}(I_T; y, \mathbf{p}, T) - \epsilon) \frac{\partial I}{\partial \phi}] \quad (6)$$

where  $I$  are images rendered from four orthogonal viewpoints  $\mathbf{p}$ ,  $\phi$  is the parameters of the 3D representation,  $g(\cdot)$  is volume rendering function. To distinguish from the previous time  $t$  of the articulate model, we refer to the time step of diffusion as  $T$ .  $w(T)$  is hyper-parameter controlling the weight of  $T$ ,  $I_T$  are sampled noisy images relative to time step  $T$ ,  $y$  is text prompt,  $\epsilon_{\theta}(I_T; y, \mathbf{p}, T)$  is noise predicted by diffusion model. Compared with single-view supervision, cross-view attention spreads the known information to unobserved views and alleviates content shifting as shown in Fig. 5(b). This allows us to use a loose prompt (such as “a cat”) and leave precise parts for the synergy between reference images and SDS.

### 3.3. Canonical Score Distillation

A straightforward way for temporal consistent articulate object generation is to supervise the model in canonical space. However, the canonical model is merely a “time-slice” of

the 4D object, as depicted in Fig. 2. Roughly supervising the canonical model without considering articulations will result in the degradation of the morphological features of the model in camera spaces (Fig. 5(c)). Additionally, unreachable points in canonical space will not be optimized, even though they will be rendered in camera space.

To mitigate these issues, we employ multi-view consistent diffusion model and propose a novel Canonical Score Distillation (CSD) to generate a 4D articulate model with both time-consistency and view-consistency. We derived CSD from Eq. (6) with a time-varied 3D representation:

$$\nabla_{\phi} \mathcal{L}_{CSD}(\theta, I_t = g(\phi)) = \mathbb{E}_{T, p, \epsilon} [w(T)(\epsilon_{\theta}(I_{t, T}; y, \mathbf{p}, T) - \epsilon) \frac{\partial I_t}{\partial \phi}] \quad (7)$$

where  $\phi$  is the parameter consisting of warping parameter  $\phi_w$  and camera space model  $\phi_*$ ,  $g(\cdot)$  is the image-level form of volume rendering (Eq. (4)).  $I_t$  are four images rendered in the camera space of time  $t$  from four orthogonal viewpoints  $\mathbf{p}$ ,  $I_{t, T}$  are sampled noisy images relative to frame time  $t$  and diffusion time step  $T$ ,  $\epsilon_{\theta}(I_{t, T}; y, \mathbf{p}, T)$  is noise predicted by diffusion model conditioned on prompt and camera poses.

Compared with vanilla SDS, CSD simplifies the generation dimension from 4D to 3D by denoising over different frames in the time-varying camera spaces while conducting the distillation process in a shared canonical space. Here we express  $\frac{\partial I_t}{\partial \phi}$  at the pixel level and then expanding it using Eq. (4) and Eq. (5):

$$\frac{\partial c_t}{\partial \phi} = \frac{\partial \mathcal{R}_{\phi_*}(\mathcal{W}_{\phi_w}^{t, \leftarrow}(\mathbf{X}^t))}{\partial \mathcal{W}_{\phi_w}^{t, \leftarrow}(\mathbf{X}^t)} \frac{\partial \mathcal{W}_{\phi_w}^{t, \leftarrow}(\mathbf{X}^t)}{\partial \phi} \quad (8)$$

As  $\mathcal{W}_{\phi_w}^{t, \leftarrow}(\mathbf{X}^t)$  are sampling points warped to canonical space via parameter  $\phi_w$ , we replace it with  $X^*$  for better understanding. The Eq. (3) states that  $\mathcal{W}_{\phi_w}^{t, \leftarrow}(\mathbf{X}^t)$  is independent of  $\phi_*$ , for it only warps the sample point from camera space to canonical space. So we have:

$$\frac{\partial c_t}{\partial \phi} = \frac{\partial \mathcal{R}_{\phi_*}(\mathbf{X}_*)}{\partial \mathbf{X}_*} \frac{\partial \mathcal{W}_{\phi_w}^{t, \leftarrow}(\mathbf{X}_t)}{\partial \phi_w} \quad (9)$$

The first term indicates that the generation is simplified from a 4D time-varying model to a 3D static canonical model. Although we traverse all camera spaces, the distillation process is consistently conducted with respect to the canonical model parameters  $\phi_*$ . Regarding the term  $\frac{\partial \mathcal{W}_{\phi_w}^{t, \leftarrow}(\mathbf{X}_t)}{\partial \phi_w}$ , it signifies that the warping parameters  $\phi_w$  are optimized to better collaborate with the canonical model in different poses (Fig. 5(c)). Therefore, by back-propagating gradients through differentiable warping, CSD optimizes a static model, similar to how vanilla SDS does. This ensures

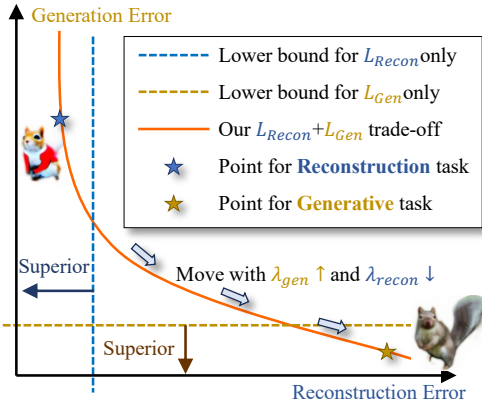


**Figure 3. Balancing generation and reconstruction trade-off.** This figure illustrates the trade-off between generation and reconstruction. As the loss weights are balanced, the optimal solution shifts from the upper-left corner towards the lower-right. Star-shaped markers indicate points of superior performance compared to utilizing only one type of loss. Notably, “Generation Error” is defined as the deviation in model quality from an ideal model.

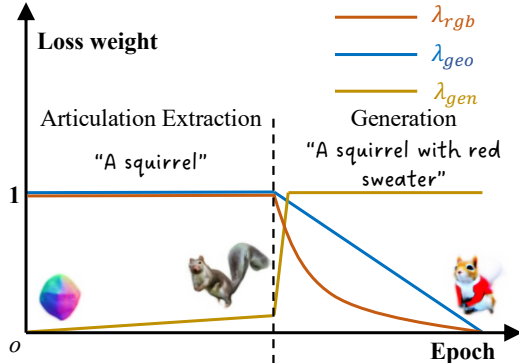


**Figure 4. Two-stage training progress.** In the first stage, we extract the articulation of the template video with CSD as a regularizer. Then we modify the prompt and gradually anneal the reconstruction loss to generate a new model.

the convergence of the model. In summary, we disentangle deformable object generation into an inductive prior-guided articulation and a diffusion-guided 3D generation, supervising a 4D representation in a spatiotemporally consistent manner.

### 3.4. Optimization

Intuitively, reconstruction and generation may seem antagonistic, as the former strives for faithful recovery of the target instance, while the latter seeks diverse outcomes based on given priors. However, with CSD (Sec. 3.3), we find that they can serve as effective mutual regularizers. This synergy exceeds the performance achievable by using only one loss type, as demonstrated in Fig. 3.

The total loss for ANIMATABLEREAMER is defined as

Eq. (10):

$$\mathcal{L} = \mathcal{L}_{recon} + \mathcal{L}_{regist} + \lambda_{gen} \mathcal{L}_{CSD}, \quad (10)$$

The weight  $\lambda_{gen}$  determines whether  $\mathcal{L}_{CSD}$  is a regularizer or a generator. The reconstruction loss  $\mathcal{L}_{recon}$  is consist of photo-metric loss  $\mathcal{L}_{rgb}$ , silhouette reconstruction  $\mathcal{L}_{sil}$  and flow loss  $\mathcal{L}_{OF}$  defined in Eq. (11):

$$\begin{aligned} \mathcal{L}_{recon} &= \lambda_{rgb} \mathcal{L}_{rgb} + \lambda_{geo} (\mathcal{L}_{sil} + \mathcal{L}_{OF}), \\ \mathcal{L}_{rgb} &= \sum_{\mathbf{x}^t} \|\mathbf{c}(\mathbf{x}^t) - \hat{\mathbf{c}}(\mathbf{x}^t)\|^2, \\ \mathcal{L}_{sil} &= \sum_{\mathbf{x}^t} \|\mathbf{o}(\mathbf{x}^t) - \hat{\mathbf{s}}(\mathbf{x}^t)\|^2, \\ \mathcal{L}_{OF} &= \sum_{\mathbf{x}^t, (t+t')} \|\mathcal{F}(\mathbf{x}^t, t \rightarrow t') - \hat{\mathcal{F}}(\mathbf{x}^t, t \rightarrow t')\|^2, \end{aligned} \quad (11)$$

where silhouette  $\mathbf{o}(\mathbf{x}^t)$  and optical flow  $\mathcal{F}(\mathbf{x}^t, t \rightarrow t')$  are pre-computed,  $\lambda_{rgb}$  and  $\lambda_{geo}$  are balancing weights. The registration loss  $\mathcal{L}_{regist}$  is defined in Eq. (12):

$$\begin{aligned} \mathcal{L}_{regist} &= \mathcal{L}_{match} + \mathcal{L}_{2D-cyc} + \mathcal{L}_{3D-cyc}, \\ \mathcal{L}_{match} &= \sum_{\mathbf{vt}} \|\hat{\mathbf{X}}^*(\mathbf{x}^t) - \mathbf{X}^*(\mathbf{x}^t)\|_2^2, \\ \mathcal{L}_{2D-cyc} &= \sum_{\mathbf{x}^t} \left\| \Pi^t \left( \mathcal{W}^{t, \rightarrow} \left( \hat{\mathbf{X}}^*(\mathbf{x}^t) \right) \right) - \mathbf{x}^t \right\|_2^2, \\ \mathcal{L}_{3D-cyc} &= \sum_i \tau_i \left\| \mathcal{W}^{t, \rightarrow} \left( \mathcal{W}^{t, \leftarrow} (\mathbf{X}_i^t) \right) - \mathbf{X}_i^t \right\|_2^2, \end{aligned} \quad (12)$$

where  $\mathcal{L}_{match}$ ,  $\mathcal{L}_{2D-cyc}$  and  $\mathcal{L}_{3D-cyc}$  are 3D point feature matching loss [47], 2D cycle consistency loss [46] and 3D cycle consistency [14].

Here, we have designed a two-stage schedule with balanced weights for generation, as depicted in Fig. 4. During the articulation extraction stage, the model is primarily supervised by images, with pre-computed depth, flow, and features. Concurrently, serving as a regularizer for reconstruction, the multi-view consistent diffusion model is provided with a prompt and configured with a low loss weight. As the articulation extraction stage concludes, we give the diffusion model a new prompt for generation and allow SDS to dominate the procedure. Meanwhile, to avoid morphological feature corruption, especially when the time step of diffusion  $T$  is large, we use the reconstruction loss as a regularizer for geometry by annealing the reconstruction loss. To perform a coarse-to-fine optimization, we increase the bandwidth coefficient of the position embedding [17] during the articulation extraction stage and then fix it during the generation stage. For the reconstruction task, we set  $\lambda_{rgb}$ ,  $\lambda_{recon}$ , and the prompt as constants, while assigning increasing values to  $\lambda_{gen}$ .

## 4. Experiments

We conducted experiments on generation (Sec. 4.2) and reconstruction (Sec. 4.3) tasks using the Casual Videos dataset and Animated Objects dataset [47]. These experiments encompassed a range of species, including squirrels, cats, finches, eagles, among others, to effectively demonstrate the generic-category capability of our method. In the context of the generation task, our method excels in creating spatiotemporally consistent, animatable 3D models with text prompts and a template video. For the reconstruction task, our approach has demonstrated superior performance over previous methods.

### 4.1. Technical Details

We implement our method on BANMo[47]. To enlarge the Casual Videos dataset [47], we collect videos containing a single complete instance with large kinesis from internet. We utilize off-the-shelf models including TrackAnything [50], ZoeDepth [3], VCN [45] and DINOV2 [19] to extract mask, depth, optical flow and features respectively. We modify the camera distance and near-far plane calculation to avoid the articulated model out of frustum or obstructing the camera. Considering that viewpoints are fixed for reconstruction and randomly selected for generation, we alternate the loss calculation of reconstruction and generation in practice. On a single Nvidia A800 GPU, we sampled 128 pixels from 32 images in reconstruction and rendered four  $88 \times 88$  images for generation. The complete training takes 3 hours for 120 iterations.

### 4.2. Text-based Animatable 3D Model Generation

We present our generated results alongside the input videos in Fig. 7. By disentangling the deformation and canonical model, our generated models demonstrate time consistency, even in cases where the video duration is extensive. Through optimization across all frames, our approach effectively eliminates issues such as disconnected shapes, flickering, and shape inconsistency. Notably, our method is capable of generating various species including quadruped, squirrel, eagle, bird, penguin and so on, and goes beyond mere texture generation with modifying the model’s geometry. Given the absence of a generic-category animatable 3D model generation method in the current landscape, we conducted a comparative analysis with several notable 3D generation and 4D reconstruction methods: Prolific-Dreamer [41], 3D reconstructor BANMo [47], texture-swap articulated representation Farm3D [12] and text to video generator Text2Video-Zero [13] and summarize our strengths in Tab. 1.

### 4.3. Animatable 3D Model Reconstruction

**Qualitative Comparisons.** As depicted in Fig. 8, we outperform the existing animatable object reconstruction

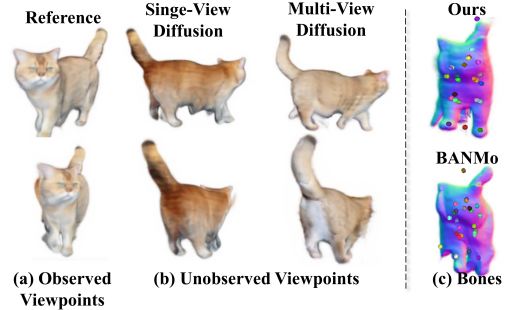


Figure 5. **Reconstruction consistency comparison of single-view SDS and multi-view SDS.** (a) Reference view. (b) In unobserved regions, multi-view diffusion achieves better texture consistency compared to single-view diffusion in reconstruction. (c) Our method results in a more logically distributed arrangement of bones (represented by colorful spheres).

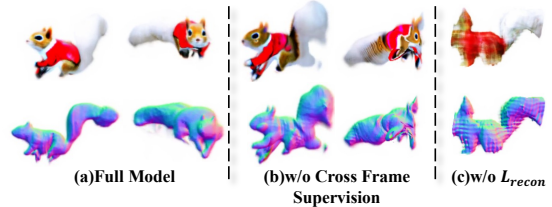


Figure 6. **Ablation study on CSD.** (a) Full model. (b) Limiting supervision solely to the canonical space leads to model corruption when extrapolated to the camera space. (c) Generating without reconstruction loss will lead to model collapsing

method on Casual Videos dataset and Animation Objects dataset (Sec. 4). A notable observation is that our approach goes beyond merely refining the canonical model. It also encompasses modifications to the bones and warping fields, as stated in Eq. (9). This comprehensive modification is especially effective in scenarios where the initial bone structures are implausible. In such cases, our method adeptly repositions the bones, accompanied by corresponding adjustments to the warping function, which is clearly evidenced in Fig. 5(c). It is evident that while BANMo delivers good results at the input views, its performance significantly diminishes in unobserved spaces. This discrepancy in quality can be attributed to the model’s tendency to overfit on the reference views, especially when there is a lack of supervision from other viewpoints, as we discussed in Fig. 2.

**Quantitative Comparisons.** Our evaluation utilizes both Chamfer distances [35] and F-scores using a threshold set to 2% of the bounding box size. Consider that Casual Videos has no ground truth, we employ BANMo on multiple video sequences and extract meshes to serve as pseudo ground truth. The result in Sec. 4.2 suggests ANIMATABLE-DREAMER significantly outperforms BANMo, even when the pseudo ground truth is derived from BANMo itself. This indicates that, with CSD, our framework effectively supple-

Method	Prompt	Category	Generation	3D Model	Motion	Articulation
Prolific-Dreamer[41]	Text	Generic	Geometry+Texture	NeRF	-	-
Text2Video-Zero[13]	Text	Generic	-	-	Learned	-
BANMo[47]	-	Generic	-	NeRF	Learned	Learned
Farm3D[12]	Image	Specific	Texture	Mesh	Hand-crafted	Pre-defined
<b>Ours</b>	<b>Video+Text</b>	<b>Generic</b>	<b>Geometry+Texture</b>	<b>NeRF</b>	<b>Learned</b>	<b>Learned</b>

Table 1. **Related work overview on non-rigid 3D model reconstruction and generation.** Distinguishing from previous work, our method, ANIMATABLEDREAMER, generates text-guided animatable models across generic categories without the need for pre-defined templates. This attribute establishes ANIMATABLEDREAMER as a versatile and user-friendly 4D generation tool.

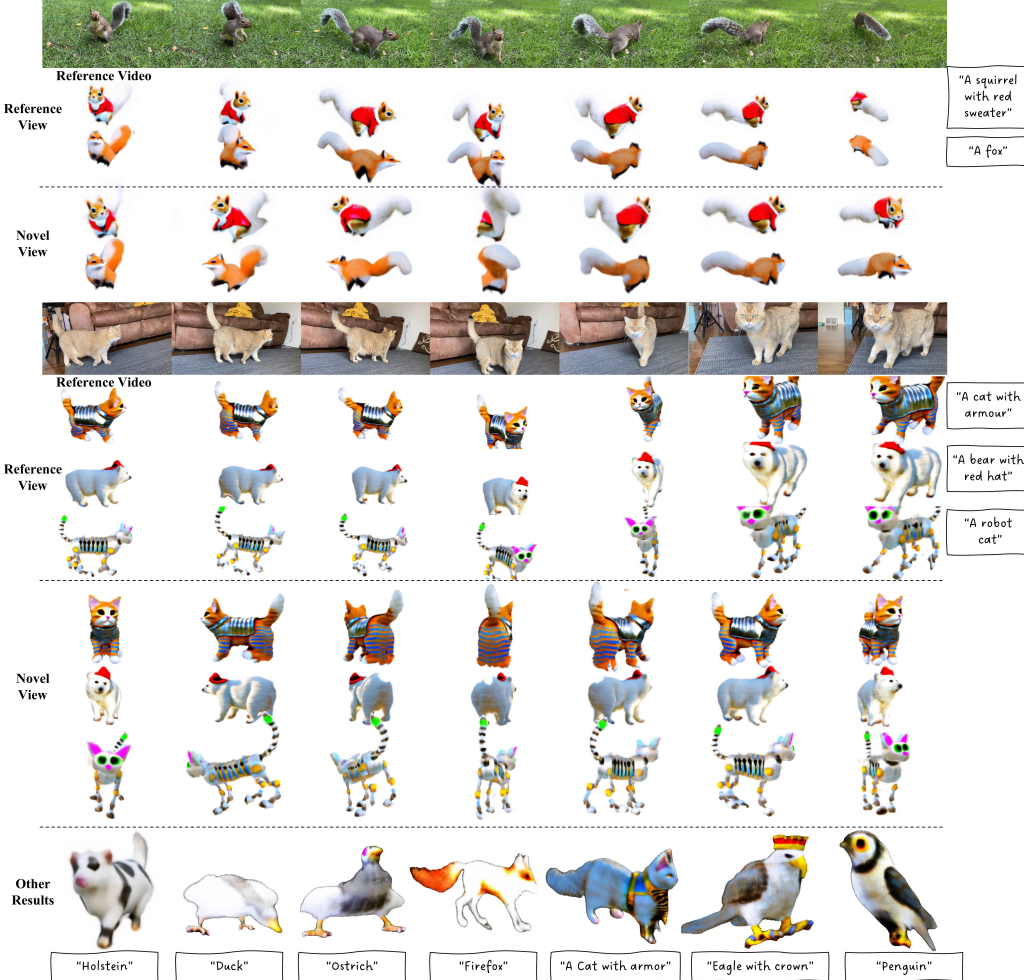


Figure 7. **Text-to-4D Generation.** We generate animatable 3D models by leveraging a text prompt and a template video, achieving diverse outcomes that encompass both texture and geometry, while maintaining temporal consistency and morphological plausibility across different poses. See Appendix for more results.

ments the missing information, surpassing the need for additional video data.

#### 4.4. Ablation Study

We ablate the importance of each component To assess the spatial consistency of multi-view diffusion, we replace CSD

with singe-view SDS DreamFusion-IF [23] to regularize the reconstruction. The result demonstrates favorable quality at viewpoints near the reference. Nevertheless, it fails to generate consistent texture when there are few observed pixels in the rendered images shown in Fig. 5(b).

In Fig. 6, we conduct ablation to evaluate the effect of

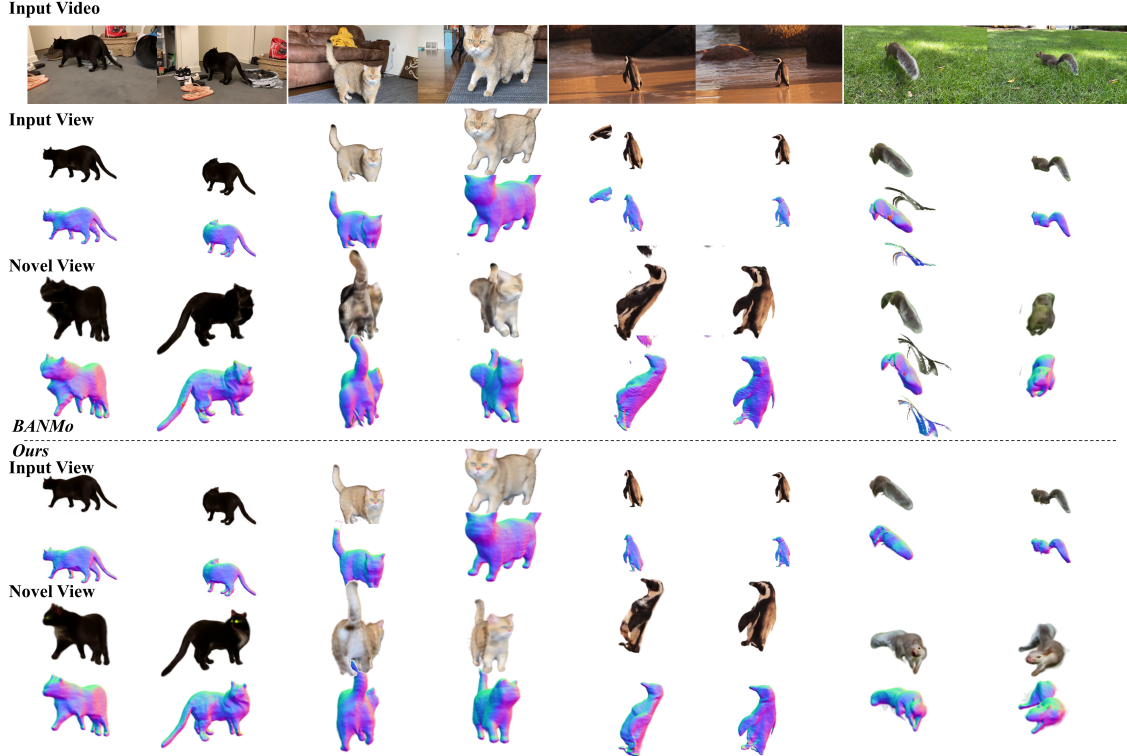


Figure 8. **Monocular reconstruction result on Casual videos dataset.** Our method is visibly superior to BANMo, particularly in frames with large motion (squirrel) or in regions not present in the reference image (cat and penguin). Each experiment is performed based on a **single monocular video**. See Appendix for more results.

Methods	Cat-Coco		Cat-Pikachu		Penguin		Shiba		Eagle	
	CD	F@%2	CD	F@%2	CD	F@%2	CD	F@%2	CD	F@%2
BANMo[47]	10.7	15.3	3.7	57.3	6.4	43.9	6.81	36.6	16.0	18.1
Ours	<b>3.65</b>	<b>63.3</b>	<b>2.0</b>	<b>88.9</b>	<b>3.7</b>	<b>64.0</b>	<b>4.54</b>	<b>53.9</b>	<b>12.8</b>	<b>21.3</b>

Table 2. **Quantitative results of monocular reconstruction on Casual Videos and Animated Objects.** We calculate the Chamfer distance (cm, ↓) and F-score (% ↑), averaging the results over all frames and videos.

supervising across different frames, demonstrating that supervising the canonical space only will cause the model corrupted in camera space. In addition, to verify the regularization effect of  $\mathcal{L}_{recon}$ , we experimentally set  $\lambda_{recon}$  to zero during training. Within a few epochs, the model experiences a collapse (Fig. 6(c)), ultimately converging to a zero SDF field.

## 5. Conclusion

In this work, we have presented ANIMATABLEDREAMER, a pioneering framework for the generation and reconstruction of generic-category non-rigid 3D models. With the proposed canonical score distillation strategy, ANIMATABLEDREAMER addresses the challenges of unconstrained deformable object generation by simplifying the 4D generation problem into 3D space. Our two-stage framework excels in generating diverse spatial-temporally consistent non-

rigid 3D models based on textual prompts. With articulations extracted from monocular video, users can manipulate and animate these models by controlling the rigid transformations of bones. Furthermore, our method surpasses the typical monocular non-rigid body reconstruction technique, especially in scenarios with limited viewpoints and substantial motion.

**Limitations.** ANIMATABLEDREAMER is not capable of rendering high-resolution images for CSD during training, due to the long gradient chain from camera space to canonical space, posing constraints on the optimization process. The requirement to feed four images into MVDream simultaneously poses a computational burden further. Addressing these issues could enhance the overall performance and versatility. Moreover, the diffusion model contributes to plausible geometry and texture in each frame but falls short in truly generating dynamic actions.

# AnimatableDreamer: Text-Guided Non-rigid 3D Model Generation and Reconstruction with Canonical Score Distillation

## Supplementary Material

### A. Multimedia Results

For more detailed and vivid results, please visit our gallery at <https://AnimatableDreamer.github.io/>.

### B. Additional Experiment Results of Animatable Model Generation

We present additional results of AnimatableDreamer for non-rigid generation in Fig. 9. AnimatableDreamer exhibits robust generalization performance across various types of non-rigid objects.

### C. Additional Experiment Results of Animatable Model Reconstruction

We present additional results of AnimatableDreamer for non-rigid reconstruction in Fig. 10. In contrast to existing methods, our framework effectively completes the unobserved regions on the 3D model, leveraging the inductive priors and instance information provided by the multi-view diffusion model.

### D. Pseudo-code for AnimatableDreamer

Here, we present the pseudo-code for AnimatableDreamer in Algorithm 1.

---

#### Algorithm 1 Pseudo-code for AnimatableDreamer

---

**Require:**  $\{I\}, \{t\}, \{p\}, c$   
**Ensure:**  $\phi$

- 1: Initialize  $\phi$
- 2: **for** each  $i \in [1, N]$  **do**
- 3:     Set position embedding bandwidth
- 4:     **if**  $i \bmod 2 == 0$  **then**
- 5:          $I, t, p \leftarrow \text{Sampler}(\{I\}, \{t\}, p)$
- 6:          $I_r \leftarrow \text{Render}(\phi, t, p)$
- 7:          $\mathcal{L} \leftarrow (\mathcal{L}_{\text{Recon}}(I_r; I) + \mathcal{L}_{\text{Regist}})$
- 8:         Optimize  $\phi$
- 9:     **else**
- 10:          $t, p, T \leftarrow \text{Sampler}(\{t\}, \text{random pose, schedule})$
- 11:          $I_r \leftarrow \text{Render}(\phi, t, p)$
- 12:          $\mathcal{L} \leftarrow (\mathcal{L}_{\text{CSD}}(I_r; t, T, p, c) + \mathcal{L}_{\text{Regist}})$
- 13:         Freeze CameraMLP, Embedder
- 14:         Optimize  $\phi$
- 15:         Unfreeze CameraMLP, Embedder
- 16: **return**  $\phi$

---

Loss	Weight	Loss	Weight
$\mathcal{L}_{\text{CSD}}$	1e-6	$\mathcal{L}_{\text{match}}$	0.01
$\mathcal{L}_{\text{rgb}}$	0.1	$\mathcal{L}_{\text{2D-cyc}}$	5e-2
$\mathcal{L}_{\text{sil}}$	0.1	$\mathcal{L}_{\text{3D-cyc}}$	5e-2
$\mathcal{L}_{\text{OF}}$	0.5		

Table 3. **Loss weight.** Here, we balance the CSD loss weight with reconstruction losses for stable generation and reconstruction.

This pseudo-code provides an overview of the CSD process, including initialization, sampling, rendering, loss calculation, and optimization steps for training the model. The Sampler function is responsible for extracting relevant information from input datasets, and the Render function generates images based on the current model parameters. The loss terms include reconstruction loss  $\mathcal{L}_{\text{Recon}}$ , CSD loss  $\mathcal{L}_{\text{CSD}}$ , and regularization loss  $\mathcal{L}_{\text{Regist}}$ . The optimization alternates between the generation and reconstruction loss functions. The CameraMLP and Embedder are frozen when loss comes from  $\mathcal{L}_{\text{Recon}}$ . The final model parameters  $\phi$  are returned after the iterations.

### E. Additional Details

**Hyper-parameters.** In the generation stage, we linearly decrease  $\lambda_{geo}$  from 1 to 0, and  $\lambda_{rgb}$  decreases following a logarithmic function from 1 to zero. For  $\lambda_{gen}$ , it linearly increases from 0 to 0.1 in the articulation extraction stage and then to 1 in the generation stage. In addition to  $\lambda$ , each loss term has its own weight to balance the magnitudes of different loss terms, as shown in Appendix E. We utilize an AdamW optimizer with a learning rate set to 5e-4.

**CSD is more CFG friendly.** For multi-view diffusion, the classifier-free guidance (CFG) weight is set to 50. In our experiments, we observe that setting CFG to around 30 yields the most beneficial results, as illustrated in Fig. 11. This observation is attributed to the fact that the reconstruction loss aids in controlling the consistency of the generated content. However, for the reconstruction task, we have observed that setting CFG to a relatively large value is beneficial, as shown in Appendix E. Therefore, we set CFG to 100 for the reconstruction process.

**CDS time step schedule.** Given that our framework is a combination of both a generator and a reconstructor, we have carefully designed the SDS time step schedule based on a series of experiments. For prompts that induce significant changes in the object’s geometry, we implement an annealing time step schedule ranging from 0.8 to 0.5. In



Figure 9. **Results of high-quality animatable models from AnimatableDreamer.** We set the background to black in some cases for better generation.

cases where the prompt primarily affects texture or involves minimal geometry changes, we sample the time step in the

range of 0 to 0.5. The impact of the SDS time step for generation is illustrated in Fig. 13. For reconstruction, we fix

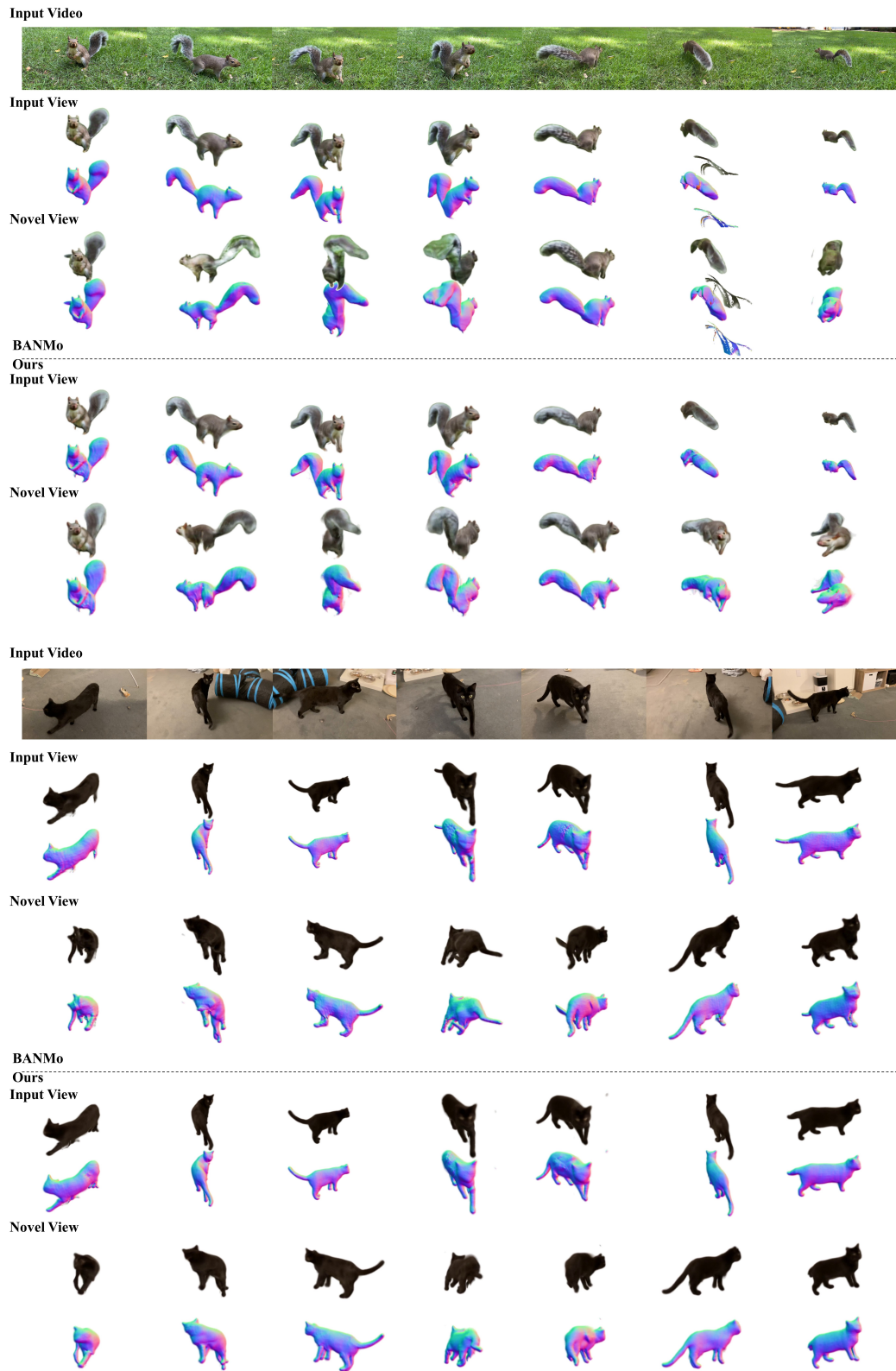


Figure 10. **Full reconstruction result.**

Guidance scale	CD	F@%2
10	5.52	44.8
30	5.33	43.7
50	5.45	45.5
100	4.6	52.1

Table 4. **Ablation of the guidance scale in reconstruction.** A large guidance scale can ensure the consistency of the reconstructed model.



Figure 11. **Influence of guidance scale.** Setting CFG to 100 enhances the mode-seeking feature and almost bypasses the generation loss, while setting CFG to 10 results in the collapse of the 3D model. This behavior may be attributed to the strong constraints imposed by the articulation extracted from the template video, rendering high CFG unnecessary for ensuring the consistency of the diffusion model.

Maximum $T$	CD	F@%2
0.5	4.6	52.1
0.8	5.06	47.8
0.98	4.68	49.1

Table 5. **Ablation of the time step schedule in reconstruction.**

the time step to 0.5 after experiments Appendix E.

**Near-far planes.** Given that we render from a free viewpoint rather than fixing on the reference, it is essential to compute the near-far plane of each frame dynamically. Therefore, our near-far planes are calculated on the fly to encompass all points of the proxy geometry with a considerable margin.

**Issue about MVDream.** MVDream is trained in a controlled environment where the object always faces the “forward” direction and is maintained at a proper distance from

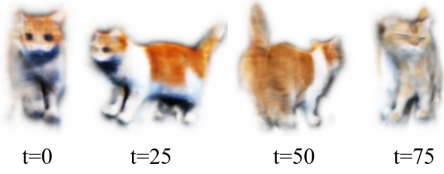


Figure 12. **Time-invariant RGB ablation.** If we set the RGB values to be time-variant, we won’t be able to cover all the points in the 4D space and consequently, the texture won’t be time-consistent. For instance, the cat’s face might look entirely different between the first frame and the last frame.

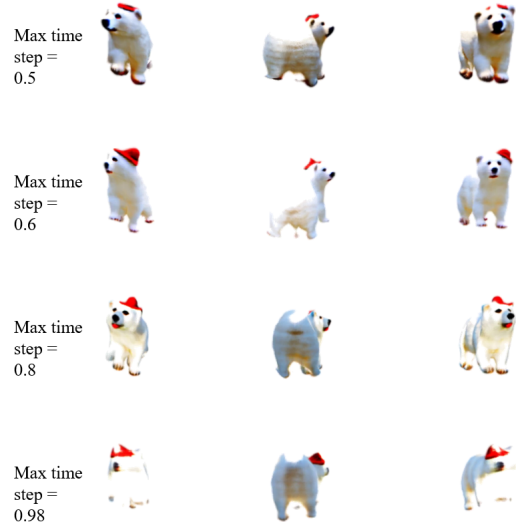


Figure 13. **The effect of the SDS time step.**

the camera. In contrast, our framework defines the “forward” direction based on the input video. To align the canonical model with the “forward” direction, we introduce an azimuth offset.

**How the number of videos impact result.** To reconstruct a complete shape with plausible skinning weights and motion, BANMo requires all object surfaces to be visible from at least one frame. However, with the induct prior for diffusion model, we can decrease the number of videos needed. In Appendix E, we report that we archive comparable results when there is only a single video.

**The prompt impact result.** We find out that adding some fixed negative prompts is helpful for our task. For example, *ugly, bad anatomy, blurry, pixelated obscure*. Besides, adding words describing the background is also helpful when the model color is similar to the background.

**Time-invariant RGB.** Setting RGB to time-invariant could provide more time-consistency to the model when we take generation loss to assist reconstruction, shown in Fig. 12.

Methods	Cat-Coco		Cat-Pikachu		Penguin		Shiba	
	CD	F@%2	CD	F@%2	CD	F@%2	CD	F@%2
BANMo (1 vid)	9.26	29.0	6.21	35.9	9.51	32.0	3.94	58.7
BANMo (2 vid)	6.78	36.9	5.79	38.4	3.88	58.3	3.44	65.9
BANMo (3 vid)	6.04	44.8	5.65	40.5	-	-	2.83	74.3
BANMo (4 vid)	4.66	51.6	4.51	52.7	-	-	2.66	77.9
Ours (1 vid)	<b>4.88</b>	<b>52.4</b>	<b>5.24</b>	<b>41.4</b>	<b>4.06</b>	<b>57.2</b>	<b>2.36</b>	<b>83.6</b>

Table 6. **Ablation of the video number.** We calculate the Chamfer distance (cm, ↓) and F-score (% ,↑), averaging the results over all frames and videos.

## References

- [1] Jonathan T Barron, Ben Mildenhall, Matthew Tancik, Peter Hedman, Ricardo Martin-Brualla, and Pratul P Srinivasan. Mip-nerf: A multiscale representation for anti-aliasing neural radiance fields. In *Proceedings of the IEEE/CVF International Conference on Computer Vision (ICCV)*, 2021. [2](#)
- [2] Jonathan T Barron, Ben Mildenhall, Dor Verbin, Pratul P Srinivasan, and Peter Hedman. Mip-nerf 360: Unbounded anti-aliased neural radiance fields. In *IEEE/CVF Conference on Computer Vision and Pattern Recognition (CVPR)*, 2022. [2](#)
- [3] Shariq Farooq Bhat, Reiner Birk, Diana Wofk, Peter Wonka, and Matthias Müller. Zoedepth: Zero-shot transfer by combining relative and metric depth, 2023. *arXiv:2302.12288 [cs]*. [6](#)
- [4] Ang Cao and Justin Johnson. Hexplane: A fast representation for dynamic scenes. In *IEEE/CVF Conference on Computer Vision and Pattern Recognition (CVPR)*, 2023. [2](#)
- [5] Rui Chen, Yongwei Chen, Ningxin Jiao, and Kui Jia. Fantasia3d: Disentangling geometry and appearance for high-quality text-to-3d content creation. *arXiv preprint arXiv:2303.13873*, 2023. [3](#)
- [6] Xu Chen, Yufeng Zheng, Michael J Black, Otmar Hilliges, and Andreas Geiger. Snarf: Differentiable forward skinning for animating non-rigid neural implicit shapes. In *Proceedings of the IEEE/CVF International Conference on Computer Vision (ICCV)*, 2021. [1](#)
- [7] Zhaoxi Chen, Guangcong Wang, and Ziwei Liu. SceneDreamer: Unbounded 3D Scene Generation from 2D Image Collections, 2023. *arXiv:2302.01330 [cs]*. [2](#)
- [8] Wei Cheng, Ruixiang Chen, Siming Fan, Wanqi Yin, Keyu Chen, Zhongang Cai, Jingbo Wang, Yang Gao, Zhengming Yu, Zhengyu Lin, et al. Dna-rendering: A diverse neural actor repository for high-fidelity human-centric rendering. In *Proceedings of the IEEE/CVF International Conference on Computer Vision (ICCV)*, 2023. [1, 2](#)
- [9] Matt Deitke, Dustin Schwenk, Jordi Salvador, Luca Weihs, Oscar Michel, Eli Vanderbilt, Ludwig Schmidt, Kiana Ehsani, Aniruddha Kembhavi, and Ali Farhadi. Objaverse: A universe of annotated 3d objects. In *IEEE/CVF Conference on Computer Vision and Pattern Recognition (CVPR)*, pages 13142–13153, 2023. [4](#)
- [10] Yilun Du, Yinan Zhang, Hong-Xing Yu, Joshua B Tenenbaum, and Jiajun Wu. Neural radiance flow for 4d view synthesis and video processing. In *Proceedings of the IEEE/CVF International Conference on Computer Vision (ICCV)*, pages 14304–14314. IEEE Computer Society, 2021. [2](#)
- [11] Sara Fridovich-Keil, Giacomo Meanti, Frederik Rahbæk Warburg, Benjamin Recht, and Angjoo Kanazawa. K-planes: Explicit radiance fields in space, time, and appearance. In *IEEE/CVF Conference on Computer Vision and Pattern Recognition (CVPR)*, pages 12479–12488, 2023. [2](#)
- [12] Tomas Jakab, Ruining Li, Shangzhe Wu, Christian Rupprecht, and Andrea Vedaldi. Farm3d: Learning articulated 3d animals by distilling 2d diffusion. *arXiv preprint arXiv:2304.10535*, 2023. [1, 6, 7](#)
- [13] Levon Khachatryan, Andranik Mousisyan, Vahram Tadevosyan, Roberto Henschel, Zhangyang Wang, Shant Navasardyan, and Humphrey Shi. Text2video-zero: Text-to-image diffusion models are zero-shot video generators. *arXiv preprint arXiv:2303.13439*, 2023. [6, 7](#)
- [14] Zhengqi Li, Simon Niklaus, Noah Snavely, and Oliver Wang. Neural scene flow fields for space-time view synthesis of dynamic scenes. In *IEEE/CVF Conference on Computer Vision and Pattern Recognition (CVPR)*, 2021. [2, 5](#)
- [15] Zhaoshuo Li, Thomas Müller, Alex Evans, Russell H Taylor, Mathias Unberath, Ming-Yu Liu, and Chen-Hsuan Lin. Neuralangelo: High-fidelity neural surface reconstruction. In *IEEE/CVF Conference on Computer Vision and Pattern Recognition (CVPR)*, 2023. [2](#)
- [16] Chen-Hsuan Lin, Jun Gao, Luming Tang, Towaki Takikawa, Xiaohui Zeng, Xun Huang, Karsten Kreis, Sanja Fidler, Ming-Yu Liu, and Tsung-Yi Lin. Magic3d: High-resolution text-to-3d content creation. In *IEEE/CVF Conference on Computer Vision and Pattern Recognition (CVPR)*, 2023. [1, 2, 3](#)

[17] Ben Mildenhall, Pratul P Srinivasan, Matthew Tancik, Jonathan T Barron, Ravi Ramamoorthi, and Ren Ng. Nerf: Representing scenes as neural radiance fields for view synthesis. *Communications of the ACM*, 65(1):99–106, 2021. [1](#), [2](#), [5](#)

[18] Michael Niemeyer, Jonathan T Barron, Ben Mildenhall, Mehdi SM Sajjadi, Andreas Geiger, and Noha Radwan. Regnerf: Regularizing neural radiance fields for view synthesis from sparse inputs. In *IEEE/CVF Conference on Computer Vision and Pattern Recognition (CVPR)*, 2022. [1](#)

[19] Maxime Oquab, Timothée Darzet, Théo Moutakanni, Huy Vo, Marc Szafraniec, Vasil Khalidov, Pierre Fernandez, Daniel Haziza, Francisco Massa, Alaaeldin El-Nouby, Mahmoud Assran, Nicolas Ballas, Wojciech Galuba, Russell Howes, Po-Yao Huang, Shang-Wen Li, Ishan Misra, Michael Rabbat, Vasu Sharma, Gabriel Synnaeve, Hu Xu, Hervé Jegou, Julien Mairal, Patrick Labatut, Armand Joulin, and Piotr Bojanowski. Dinov2: Learning robust visual features without supervision, 2023. [2](#), [3](#), [6](#)

[20] Keunhong Park, Utkarsh Sinha, Jonathan T Barron, Sofien Bouaziz, Dan B Goldman, Steven M Seitz, and Ricardo Martin-Brualla. Nerfies: Deformable neural radiance fields. In *Proceedings of the IEEE/CVF International Conference on Computer Vision (ICCV)*, pages 5865–5874, 2021. [1](#), [2](#)

[21] Keunhong Park, Utkarsh Sinha, Peter Hedman, Jonathan T Barron, Sofien Bouaziz, Dan B Goldman, Ricardo Martin-Brualla, and Steven M Seitz. Hypernerf: A higher-dimensional representation for topologically varying neural radiance fields. *arXiv preprint arXiv:2106.13228*, 2021. [1](#), [2](#)

[22] Sida Peng, Yuanqing Zhang, Yinghao Xu, Qianqian Wang, Qing Shuai, Hujun Bao, and Xiaowei Zhou. Neural body: Implicit neural representations with structured latent codes for novel view synthesis of dynamic humans. In *IEEE/CVF Conference on Computer Vision and Pattern Recognition (CVPR)*, 2021. [2](#)

[23] Ben Poole, Ajay Jain, Jonathan T Barron, and Ben Mildenhall. Dreamfusion: Text-to-3d using 2d diffusion. *arXiv preprint arXiv:2209.14988*, 2022. [1](#), [2](#), [3](#), [7](#)

[24] Albert Pumarola, Enric Corona, Gerard Pons-Moll, and Francesc Moreno-Noguer. D-NeRF: Neural Radiance Fields for Dynamic Scenes. In *2021 IEEE/CVF Conference on Computer Vision and Pattern Recognition (CVPR)*, pages 10313–10322, Nashville, TN, USA, 2021. IEEE. [2](#)

[25] Robin Rombach, Andreas Blattmann, Dominik Lorenz, Patrick Esser, and Björn Ommer. High-resolution image synthesis with latent diffusion models. In *IEEE/CVF Conference on Computer Vision and Pattern Recognition (CVPR)*, 2022. [1](#)

[26] Chitwan Saharia, William Chan, Saurabh Saxena, Lala Li, Jay Whang, Emily L Denton, Kamyar Ghasemipour, Raphael Gontijo Lopes, Burcu Karagol Ayan, Tim Salimans, et al. Photorealistic text-to-image diffusion models with deep language understanding. *Advances in Neural Information Processing Systems (NeurIPS)*, 2022. [1](#)

[27] Christoph Schuhmann, Romain Beaumont, Richard Vencu, Cade Gordon, Ross Wightman, Mehdi Cherti, Theo Coombes, Aarush Katta, Clayton Mullis, Mitchell Wortsman, et al. Laion-5b: An open large-scale dataset for training next generation image-text models. *Advances in Neural Information Processing Systems (NeurIPS)*, 35:25278–25294, 2022. [4](#)

[28] Ruizhi Shao, Zerong Zheng, Hanzhang Tu, Boning Liu, Hongwen Zhang, and Yebin Liu. Tensor4D: Efficient Neural 4D Decomposition for High-Fidelity Dynamic Reconstruction and Rendering. In *IEEE/CVF Conference on Computer Vision and Pattern Recognition (CVPR)*, pages 16632–16642, Vancouver, BC, Canada, 2023. IEEE. [2](#)

[29] Tianshang Shen, Jun Gao, Kangxue Yin, Ming-Yu Liu, and Sanja Fidler. Deep marching tetrahedra: a hybrid representation for high-resolution 3d shape synthesis. In *Advances in Neural Information Processing Systems (NeurIPS)*, 2021. [2](#)

[30] Yichun Shi, Peng Wang, Jianglong Ye, Mai Long, Kewei Li, and Xiao Yang. Mvdream: Multi-view diffusion for 3d generation. *arXiv preprint arXiv:2308.16512*, 2023. [1](#), [2](#), [4](#)

[31] Uriel Singer, Shelly Sheynin, Adam Polyak, Oron Ashual, Iurii Makarov, Filippos Kokkinos, Naman Goyal, Andrea Vedaldi, Devi Parikh, Justin Johnson, and Yaniv Taigman. Text-To-4D Dynamic Scene Generation, 2023. *arXiv:2301.11280 [cs]*. [2](#)

[32] Anastasis Stathopoulos, Georgios Pavlakos, Ligong Han, and Dimitris N Metaxas. Learning articulated shape with keypoint pseudo-labels from web images. In *IEEE/CVF Conference on Computer Vision and Pattern Recognition (CVPR)*, pages 13092–13101, 2023. [1](#)

[33] Shih-Yang Su, Frank Yu, Michael Zollhöfer, and Helge Rhodin. A-nerf: Articulated neural radiance fields for learning human shape, appearance, and pose. In *Advances in Neural Information Processing Systems (NeurIPS)*, 2021. [1](#)

[34] Jiaxiang Tang, Jiawei Ren, Hang Zhou, Ziwei Liu, and Gang Zeng. Dreamgaussian: Generative gaussian splatting for efficient 3d content creation. *arXiv preprint arXiv:2309.16653*, 2023. [1](#)

[35] Maxim Tatarchenko, Stephan R Richter, René Ranftl, Zhuwen Li, Vladlen Koltun, and Thomas Brox. What do single-view 3d reconstruction networks learn? In *IEEE/CVF Conference on Computer Vision and Pattern Recognition (CVPR)*, 2019. 6

[36] Haochen Wang, Xiaodan Du, Jiahao Li, Raymond A. Yeh, and Greg Shakhnarovich. Score Jacobian Chain-ing: Lifting Pretrained 2D Diffusion Models for 3D Generation, 2022. arXiv:2212.00774 [cs]. 2

[37] Liao Wang, Jiakai Zhang, Xinhang Liu, Fuqiang Zhao, Yanshun Zhang, Yingliang Zhang, Minye Wu, Jingyi Yu, and Lan Xu. Fourier plenoctrees for dynamic radiance field rendering in real-time. In *IEEE/CVF Conference on Computer Vision and Pattern Recognition (CVPR)*, 2022. 1

[38] Peng Wang, Lingjie Liu, Yuan Liu, Christian Theobalt, Taku Komura, and Wenping Wang. Neus: Learning neural implicit surfaces by volume rendering for multi-view reconstruction. *Advances in Neural Information Processing Systems (NeurIPS)*, 2021. 3

[39] Yikai Wang, Yinpeng Dong, Fuchun Sun, and Xiao Yang. Root pose decomposition towards generic non-rigid 3d reconstruction with monocular videos. In *Proceedings of the IEEE/CVF International Conference on Computer Vision (ICCV)*, 2023. 2

[40] Yiming Wang, Qin Han, Marc Habermann, Kostas Daniilidis, Christian Theobalt, and Lingjie Liu. Neus2: Fast learning of neural implicit surfaces for multi-view reconstruction. In *Proceedings of the IEEE/CVF International Conference on Computer Vision (ICCV)*, 2023. 3

[41] Zhengyi Wang, Cheng Lu, Yikai Wang, Fan Bao, Chongxuan Li, Hang Su, and Jun Zhu. Prolific-dreamer: High-fidelity and diverse text-to-3d generation with variational score distillation. *arXiv preprint arXiv:2305.16213*, 2023. 1, 2, 3, 6, 7

[42] Guanjun Wu, Taoran Yi, Jiemin Fang, Lingxi Xie, Xiaopeng Zhang, Wei Wei, Wenyu Liu, Qi Tian, and Xinggang Wang. 4D Gaussian Splatting for Real-Time Dynamic Scene Rendering, 2023. arXiv:2310.08528 [cs]. 2

[43] Shangzhe Wu, Ruining Li, Tomas Jakab, Christian Rupprecht, and Andrea Vedaldi. Magicpony: Learning articulated 3d animals in the wild. In *IEEE/CVF Conference on Computer Vision and Pattern Recognition (CVPR)*, 2023. 1

[44] Wenqi Xian, Jia-Bin Huang, Johannes Kopf, and Changil Kim. Space-time neural irradiance fields for free-viewpoint video. In *IEEE/CVF Conference on Computer Vision and Pattern Recognition (CVPR)*, pages 9421–9431, 2021. 2

[45] Gengshan Yang and Deva Ramanan. Learning to segment rigid motions from two frames. In *IEEE/CVF Conference on Computer Vision and Pattern Recognition (CVPR)*, 2021. 6

[46] Gengshan Yang, Deqing Sun, Varun Jampani, Daniel Vlasic, Forrester Cole, Ce Liu, and Deva Ramanan. Viser: Video-specific surface embeddings for articulated 3d shape reconstruction. *Advances in Neural Information Processing Systems (NeurIPS)*, 2021. 2, 5

[47] Gengshan Yang, Minh Vo, Natalia Neverova, Deva Ramanan, Andrea Vedaldi, and Hanbyul Joo. Banmo: Building animatable 3d neural models from many causal videos. In *IEEE/CVF Conference on Computer Vision and Pattern Recognition (CVPR)*, 2022. 1, 2, 5, 6, 7, 8

[48] Gengshan Yang, Chaoyang Wang, N Dinesh Reddy, and Deva Ramanan. Reconstructing animatable categories from videos. In *IEEE/CVF Conference on Computer Vision and Pattern Recognition (CVPR)*, 2023. 1

[49] Gengshan Yang, Shuo Yang, John Z. Zhang, Zachary Manchester, and Deva Ramanan. Ppr: Physically plausible reconstruction from monocular videos. In *Proceedings of the IEEE/CVF International Conference on Computer Vision (ICCV)*, pages 3914–3924, 2023. 2

[50] Jinyu Yang, Mingqi Gao, Zhe Li, Shang Gao, Fangjing Wang, and Feng Zheng. Track anything: Segment anything meets videos, 2023. 6

[51] Chun-Han Yao, Amit Raj, Wei-Chih Hung, Yuanzhen Li, Michael Rubinstein, Ming-Hsuan Yang, and Varun Jampani. Artic3d: Learning robust articulated 3d shapes from noisy web image collections. *arXiv preprint arXiv:2306.04619*, 2023. 1

[52] Lvmin Zhang, Anyi Rao, and Maneesh Agrawala. Adding conditional control to text-to-image diffusion models. In *Proceedings of the IEEE/CVF International Conference on Computer Vision (ICCV)*, 2023. 1